

FULL ARTICLE

Portable optical-resolution photoacoustic microscopy for volumetric imaging of multiscale organisms

Tian Jin¹ | Heng Guo¹ | Lei Yao^{1,2} | Huikai Xie³ | Huabei Jiang^{1,2,4*} | Lei Xi^{1,2*} 

¹School of Physical Electronics, University of Electronic Science and Technology of China, Chengdu, China

²Center for Information in Biomedicine, University of Electronic Science and Technology of China, Chengdu, China

³Department of Electrical and Computer Engineering, University of Florida, Gainesville, Florida

⁴Department of Medical Engineering, University of South Florida, Tampa, Florida

***Correspondence**

Huabei Jiang, Department of Medical Engineering, University of South Florida, Tampa, FL 33620.

Email: hjiang1@usf.edu

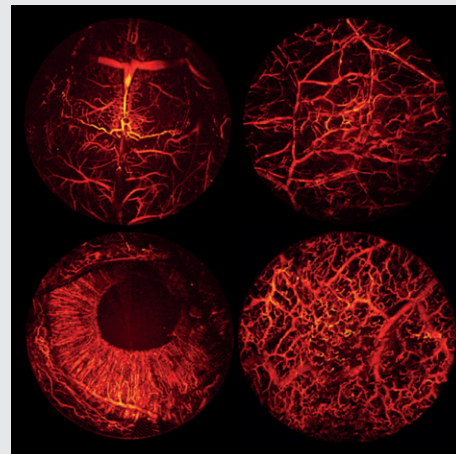
Lei Xi, School of Physical Electronics, University of Electronic Science and Technology of China, Chengdu, 610054, China.

Email: xilei1985@uestc.edu.cn

Funding information

National Natural Science Foundation of China, Grant/Award numbers: 81571722, 61775028, 61528401; Department of Science and Technology of Sichuan Province, Grant/Award number: 2016HH0019; University of Electronic Science and Technology of China, Grant/Award number: A03012023601011

Photoacoustic microscopy (PAM) provides a fundamentally new tool for a broad range of studies of biological structures and functions. However, the use of PAM has been largely limited to small vertebrates due to the large size/weight and the inconvenience of the equipment. Here, we describe a portable optical-resolution photoacoustic microscopy (pORPAM) system for 3-dimensional (3D) imaging of small-to-large rodents and humans with a high spatiotemporal resolution and a large field of view. We show extensive applications of pORPAM to multiscale animals including mice and rabbits. In addition, we image the 3D vascular networks of human lips, and demonstrate the feasibility of pORPAM to observe the recovery process of oral ulcer and cancer-associated capillary loops in human oral cavities. This technology is promising for broad biomedical studies from fundamental biology to clinical diseases.

**KEYWORDS**

portable photoacoustic microscopy, optical resolution photoacoustic microscopy

1 | INTRODUCTION

Optical imaging plays an important role in general biomedical studies from fundamental research to clinical diseases [1, 2]. However, suffering from the high optical scattering property of biological tissue, it remains an essential tradeoff between spatial resolution and imaging depth. Photoacoustic (PA) imaging (PAI), a new hybrid imaging modality owning rich optical contrast, high scalable ultrasonic resolution and deep penetration capability, overcomes the limitations of pure optical imaging modalities [3–10] and demonstrates extensive biomedical/clinical applications [11–15]. PA microscopy (PAM), a variation of PAI, scans either a focused ultrasound detector or a converging laser beam to

form an image through sequentially and directly back-projecting the depth-resolved PA signals [16, 17]. When a focused laser beam is used, it is termed as optical-resolution PA microscopy (ORPAM). ORPAM has a high lateral resolution and processes a better penetration depth compared to optical microscopies. However, conventional ORPAMs, employing mechanical raster scanning of optical and acoustic focuses, suffer from a low imaging speed and translation of samples/imaging interfaces [18, 19]. Recent progress in new acoustic/optical scanning mechanisms and ultrafast pulsed lasers promotes the development of high-speed and compact ORPAMs [20–28]. One encouraging approach introduces water-immersed magnetic micro-mirrors capable of scanning both optical and acoustic focuses to achieve

portable configurations of ORPAM [20]. Another study integrates an imaging bundle and a graded-index lens to realize a miniaturized handheld ORPAM probe [22]. However, both approaches suffer from limited field of views (FOVs) and motion artifacts induced by hands, which lead to potential image deterioration. Integrating large-area flat transducers with pure optical raster scanning can avoid mechanical translation and achieve a high temporal resolution. However, it suffers from a low signal-to-noise ratio (SNR) and a severely imbalanced sensitivity over the FOV [23, 24]. Combining hybrid scanning mechanisms with ultrafast lasers has been implemented to achieve an ultra-high temporal resolution within a small FOV which can be extended via multiple mechanical scans [25–27]. In this case, the mechanical translation inherently limits both acquisition speed and types of in vivo samples. Hence, there remain 2 major challenges for ORPAM: (1) a portable optical-resolution PA microscopy (pORPAM) that can be used for studying all-size rodents and further humans with a satisfying imaging quality and (2) an encouraging clinical application which can promote the clinical translation of ORPAM.

Here, we report a portable ORPAM system that uses a combination of 3 innovations. First, no translation of samples/imaging interfaces is required using the novel optical/acoustic scanning mechanism which enables wide-field high-quality imaging with a large depth of field (DOF). Second, multiscale resolving capability makes it accessible to multiscale organisms in both biological and clinical studies.

Finally, the compact and portable configuration provides access to medium- and large-sized rodents as well as humans. In this study, we display extensive applications of pORPAM from small- to medium-sized rodents, and further demonstrate the feasibility of this technique for oral inspection of human oral cavities.

2 | METHODS

2.1 | Imaging system

Figure S1, Supporting Information shows the schematic of the system. A Q-switched pulsed laser (FQS-200-1-532; Elforlight Ltd., Northants, UK) emits 532 nm light pulses at a maximum repetition rate of 20 000 Hz. Light pulses pass through an optical spatial filter system (KT310/M; Thorlabs Inc., New Jersey, USA), coupled into a single-mode fiber (SMF) with a free space to fiber coupler (APFC-5 T-FC; Zolix Instruments Ltd., Beijing, China), and collimated via a fiber collimator (F220FC-532; Thorlabs Inc.). A fast 2-dimensional galvanometer scanner (GVS002; Thorlabs Inc.), driven by a multifunctional analog output device (PCI-6731; National Instrument, Texas), scans collimated light on the back of the imaging lens (Figure 1A). A scan lens (LSM-03-VIS; Thorlabs Inc.) and a microscopic objective (RMS4; Thorlabs Inc.) are manually switched to focus the light beam in low- and high-resolution modes, respectively. The measured energy of the laser pluses after the

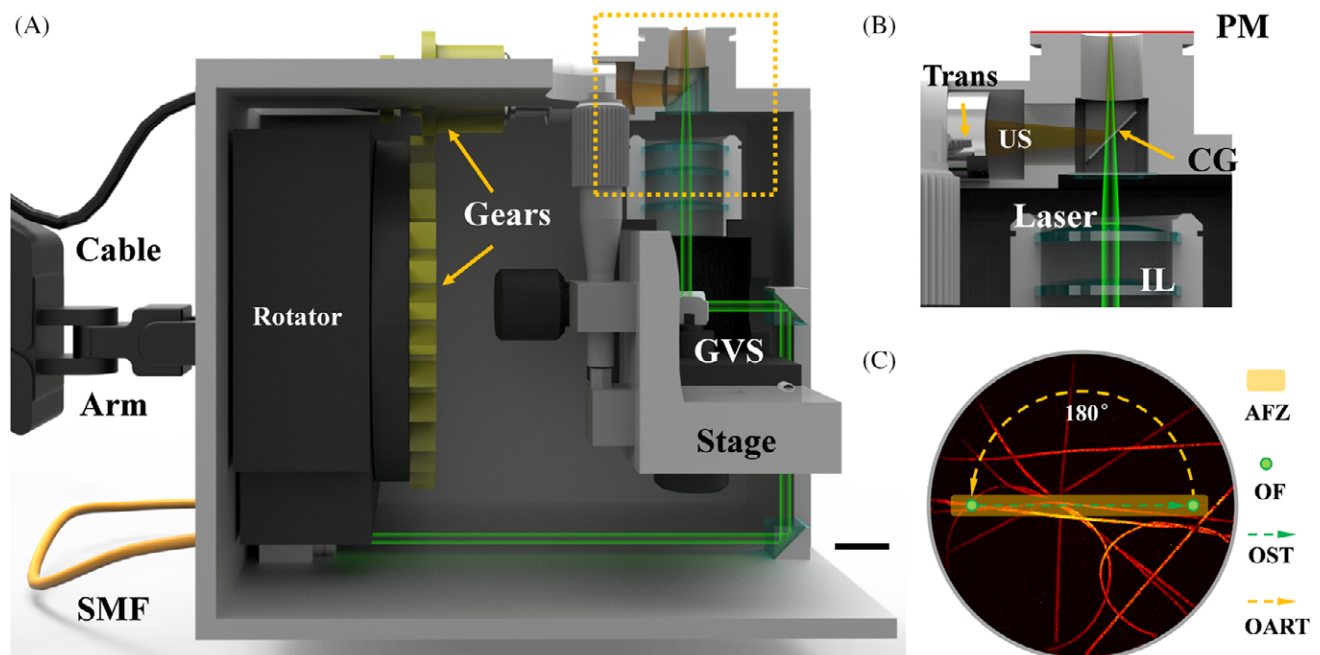


FIGURE 1 pORPAM imaging interface and the scanning mechanism. (A) Illustration of pORPAM's imaging interface. Scale bar: 1.5 cm. (B) Close-up view of the imaging interface. Two cover glasses with a thickness of 100 μm are used. The horizontal one is used to prevent the water leak. The one tilted with an angle of 45° enables the transmission of light and reflection of ultrasound. The top surface of the imaging interface is sealed with an ultrathin plastic membrane allowing fully optical and acoustic transmission. (C) Schematic of the scanning mechanism. AFZ, acoustic focal zone; CG, cover glass; GVS, galvanometer scanner; IL, imaging lens; OART, optical and acoustic rotational trace; OF, optical focus; OSL, optical scan trace; PM, plastic membrane; SMF, single-mode fiber; trans, transducer; US, ultrasound wave. Scale bar: 1.5 cm

imaging lenses is 80 nJ. The cover glass tilted with an angle of 45° in Figure 1B allows the transmission of the light to the sample, and the reflection of the light-induced ultrasound to a cylindrically focused acoustic transducer. A motorized rotator (RSA-100; Zolix Inc.) equipped with a customized accelerating gear group with a ratio of 1:4 is used to rotate the transducers in a speed of up to 180° per second. A rotatory joint is used to avoid the twist of the cable during the rotation. Figure 1C depicts the optical and acoustic scanning mechanism in detail. The focal zone of a cylindrically focused transducer (the orange bar in Figure 1C) is overlapped with the optical focal planes of the scan lenses to obtain the best SNR of PA signals. The optical focus scans in line (the dashed green arrow in Figure 1C) to form a cross-sectional slice named B-scan. Both acoustic focal zone and optical scan trace continuously rotate with a given angle until the entire imaging area is full covered (the dashed orange arrow in Figure 1C). No translation of samples/imaging interfaces is required and 1 full volume is acquired with a 180° angular rotation of acoustic focal zone and optical scan trace. Movie S1 shows an animation depicting the scanning mechanism of pORPAM.

In the high-resolution mode, a transducer (V324-SU; Olympus IMS) with a focal length of 38 mm, a center frequency of 25 MHz, an aperture of 6 mm in diameter and a bandwidth of 75% is used. In the low-resolution mode, a transducer (V319-SU; Olympus IMS) owning a focal length of 38 mm, a center frequency of 15 MHz and an aperture of 12.7 mm is utilized. The PA signals are amplified by ~39 dB using an amplifier (5073PR; Olympus IMS) and digitized using a data acquisition card (NI-5124; National Instrument) at a sampling rate of 200 MS/s.

2.2 | Phantom preparations

In order to evaluate the resolution and SNR of the system, tissue mimicking background phantoms were prepared by mixing agarose, intralipid and India ink with an optical absorption coefficient of 0.01 mm⁻¹ and a reduced scattering coefficient of 1.0 mm⁻¹. We vertically inserted a sharp blade into the phantom and tilted it with an angle of 15° to simulate an ideal edge in different depths. In low-resolution mode, we collected 1400 A-lines with an interval of 5 μm in a B-scan, and 1800 B-scans with an angular interval of 0.1° in a volume image. When switched to the high-resolution mode, we collected 2000 A-lines with a 1.5 μm interval to form a B-scan, and 3600 B-scans with a 0.05° rotational angle to reconstruct a 3-dimensional (3D) image.

2.3 | Animal preparation

All procedures in animal experiments have been approved by the Institutional Animal Care and Use Committee at the University of Electrical Science and Technology of China.

2.4 | In vivo mouse imaging

Mice (6- to 8-week-old, BALB/C) were freely laid down on a heating pad to maintain the body temperature at 37°C. A mixture of isoflurane and oxygen continually flowed over a nose mask into the mice to keep them anesthetized. The ears and brains of mice were gently depilated. The scalps were carefully removed using a surgical blade for brain imaging. Both high- and low- resolution experiments were carried out.

2.5 | In vivo rabbit imaging

Two 6-month adult and two 2-week New Zealand Male rabbits were chosen for this study. The rabbits were anesthetized by injecting pentobarbital via ear margin intravenous (30 mg/kg) and kept motionless during the experiments using 2% isoflurane and air. The ear was gently depilated to remove the influence of hairs. The rabbits were freely prostrated on a heating pad which maintained the body temperature at 37°C. We adjusted the imaging interface to fit the postures of rabbits. We imaged the rabbit eyes and ears using the low-resolution mode. No obvious damage was observed in the ear and eye after the experiments.

2.6 | In vivo human imaging

We imaged the lips of 3 male volunteers using the low-resolution mode. One had a self-developed ulcer on the lip, and 3 experiments were conducted with an interval of 24 hours. The volunteers sat on a chair and we adjusted the imaging interface to fit the posture of the volunteers. Drinkable water served as the coupling medium for acoustic transmission. After the experiments, dentists examined the imaged area for 7 days and no abnormal symptom was observed. We have obtained consents from all the volunteers participating in the experiments.

2.7 | Data acquisition and imaging processing

We carried out low-resolution experiments by collecting 700 A-lines with a step interval of 10 μm and 900 B-scans with an angular interval of 0.18°, and high-resolution experiments by acquiring 1000 A-lines with a step interval of 3.6 μm and 1000 B-scans with an angular interval of 0.18°. The volume rate is equal to the laser repetition rate divided by the number of scanning points. Our current laser can emit 20 000 pulses/s, such that an experiment for in vivo high- and low-resolution experiments would cost 50 and 35 seconds, respectively. For phantom experiments, the frame sizes for low- and high-resolution images were 1400 × 1800 and 2000 × 1800, which costed 140 and 200 seconds, respectively.

The visualization and data analysis were performed using MATLAB (MathWorks, Inc.) and Amira (Visage Imaging). We did Hilbert transform of original A-lines,

which were filtered using a 20 MHz low-pass filter. Volumetric images were reconstructed by directly back-projecting each post-processing A-line in the polar coordinate with interpolation and exhibited the volume data in maximum amplitude projection (MAP). Due to the inhomogeneous sampling pattern of the scanning mechanism, we calculated weighting factors based on the number of scans in each pixel to remove the non-uniformity of the reconstructed images. 3D renderings in the figures and movies were generated using volren modules in Amira using VolrenRed colormaps.

3 | RESULTS

3.1 | System performance

This scanning geometry provides a variable cylindrical FOV of 8.4 mm in diameter and 1.5 mm in depth for low-resolution mode, and 3.6 mm in diameter and 0.7 mm in depth for high-resolution mode. The sharp edge of the blade was imaged by pORPAM to estimate the lateral resolutions, axial resolutions and variation of PA amplitudes in depths. Figure 2A presents the lateral resolutions at the focal plane for low-resolution mode (blue dotted line) and high-resolution mode (green dotted line). Lateral resolutions are calculated by deriving the line spread functions (LSFs) from the edge spread functions of the imaged blade edge. The axial resolutions are estimated through the full-width at half-maximum (FWHM) of the Gaussian-fitted axial profiles. In the low- and high-resolution mode, the FWHMs of the LSFs are calculated as 10.8 and 4.2 μm , which lead to

energy densities of 87 and 577 mJ/cm^2 at the optical focuses in water, respectively. In the *in vivo* experiments, the focal plane is adjusted to be $\sim 500 \mu\text{m}$ under the tissue surface. Due to the high optical scattering property of the biological tissue, the photon density in the imaging plane is much lower than the American National Standards Institute safety limit of 22 mJ/cm^2 . As shown in Figure 2B, the axial resolutions are 90 and 60 μm , respectively.

With the increase of the imaging depth, the lateral resolution of high-resolution mode deteriorates rapidly and becomes worse than the one of low-resolution mode when the imaging depth is larger than 0.5 mm (Figure 2C). However, no obvious deteriorations of axial resolutions in both modes are observed. Figure 2D presents the amplitudes of PA signals obtained in different depths. Due to the scattering property of the tissue-mimicking phantom, the SNRs of both modes become worse as expected. The SNR of high-resolution mode decreases more rapidly due to a tighter focused spot and a shorter DOF.

3.2 | In vivo imaging of small rodents

To evaluate the performance of pORPAM in classical animals, we carried out *in vivo* experiments of mouse brain and ear. Figure S2 shows the photographs of a mouse in the experiments for imaging the brain and ear. Figure 3A presents the MAP image of a typical mouse ear. Figure 3B presents the MAP images of a typical mouse brain in low- and high-resolution modes. In the low-resolution mode, the complicated vascular networks can be clearly visualized in an FOV of 7 mm, yet there remain discontinued capillaries

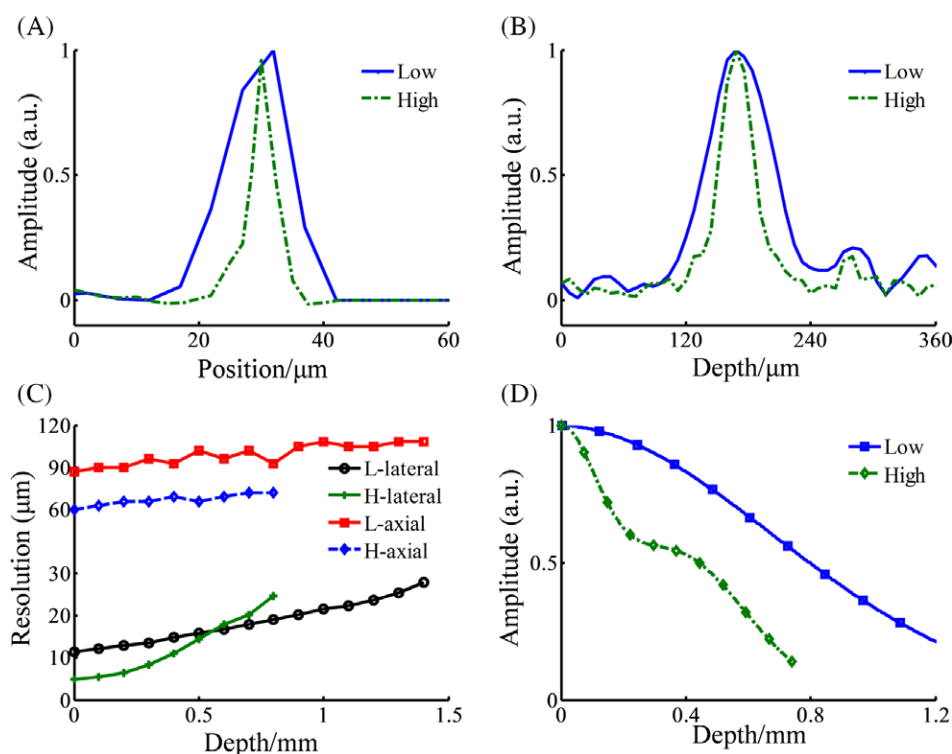


FIGURE 2 Experimental evaluation of resolution and SNR for low- and high-resolution modes. (A) Lateral resolutions of low-resolution (blue lines) and high-resolution (green lines) modes. (B) Axial resolutions of low-resolution (blue lines) and high-resolution (green lines) modes. (C) Deviations of resolutions in depths for both modes. (D) Amplitude variation of PA signals in depths for both modes

due to the limited resolving capability. In comparison, the high-resolution mode produces clearly better capillaries with a finer resolving ability and higher SNR in an FOV of 3.6 mm. Figure 3C depicts low-resolution (top) and high-resolution (bottom) volume renderings of the mouse brain. Movies S2 and S3 show the datasets in detail, including volumetric structures in different views and sequential cross-sectional slices at different depths.

3.3 | In vivo imaging of medium rodents

Medium-size rodents remain as a challenge for conventional ORPAMs. Figure 4A presents the photographs of the rabbit ear and eye imaged by pORPAM. The MAP image of the vascular network in the rabbit ear is shown in Figure 4B. Figure 4C and D presents the ophthalmic vascular network of a 2-week rabbit and a 6-month adult rabbit in vivo, respectively. pORPAM clearly visualizes and identifies the vasculatures in the iris, eyelid and sclera located at different depths. The rabbit eye ball has a highly convex curved surface, which leads to challenges for most existing ORPAM techniques due to their limited working distances, DOFs and FOVs. In addition, it is difficult to mount a rabbit on a mechanical scanner to perform raster scanning stably. The pORPAM imaging interface is flexible enough to fit the postures of rabbits. It has a sufficient DOF of up to 1.5 mm and a maximum FOV of 8.4 mm to cover the entire eye ball of a 2-week old rabbit and half of the eyeball of an adult rabbit.

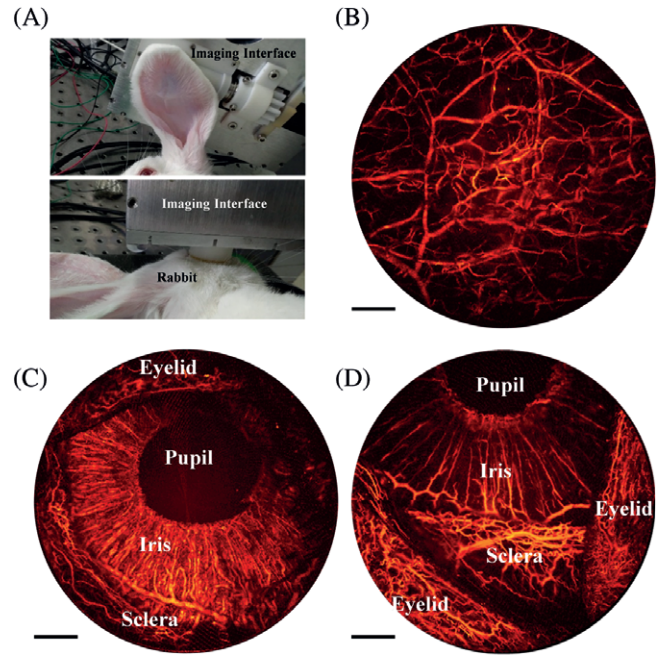
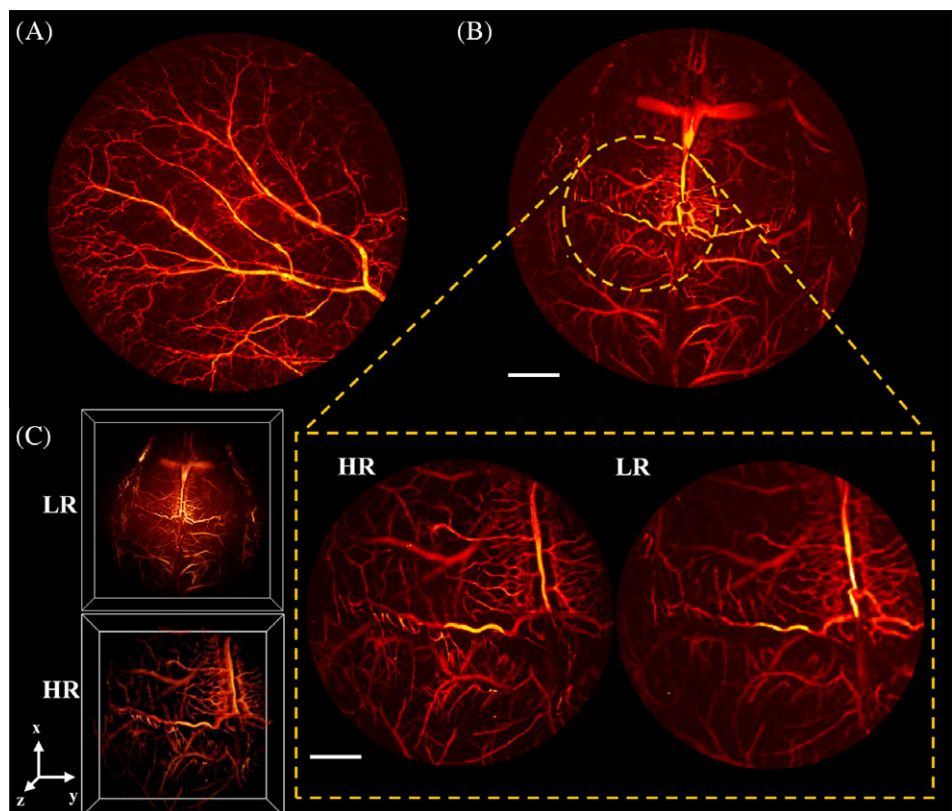


FIGURE 4 pORPAM of rabbit ears and eyes in vivo. (A) Photographs of rabbits in the experiments for imaging the ear and eye. (B) The MAP image of a rabbit ear. (C and D) pORPAM MAP images of the vasculatures in the iris, sclera and eyelid of a 2-week-old rabbit and an adult rabbit. Limited by the maximum FOV of pORPAM, partial vasculatures of an adult rabbit eye are covered. Scale bars: 1 mm

3.4 | In vivo imaging of humans

One of the major challenges for ORPAMs is the lack of a proper clinical application, which prevents its clinical

FIGURE 3 pORPAM imaging of a mouse ear and brain in vivo. (A) pORPAM image of a depilated mouse ear. (B) The low-resolution mode MAP image of the vascular structures in a mouse brain with the scalp removed in vivo (top panel). A sub-area indicated by a dashed circle imaged by both the high- and low-resolution modes. (C) Volume rendering (Amira VolrenRed) of the mouse brain acquired in low- and high-resolution modes. HR, high resolution; LR, low resolution. Scale bars: 1 mm



translation. It is known that there are ultrahigh dense vascular networks in human oral cavity. Structural and functional changes of vasculatures in the oral cavity are tightly associated with numerous diseases such as oral ulcer, oral cancer, cardiovascular abnormalities and hemorrhagic shock in humans [28]. Here, we successfully demonstrate the clinical feasibility of pORPAM in oral vascular imaging. Figure 5A shows the MAP image of the lip vascular network in a healthy volunteer, from which we clearly see ultradense vasculatures inside the lip. Movie S4 shows the volume rendering of the vasculature and sequential cross-sectional slices at different depths. From the movie, we can observe a lot of capillary loops which would bend and twist at the early stage of oral cancers within 0.1 mm volume below the lip surface [32, 33]. Figure 5B presents a recovery procedure of a lip ulcer. We observed a clear wound in which superficial vasculatures disappeared in day 1, and the growth of blood vessels in the wound from the boundary during the recovery in days 2 and 3.

4 | DISCUSSION

pORPAM is a new, wide-field, and high-speed volumetric microscopy approach capable of imaging vascular structures in a wide range of organisms. Its easy-to-use, multiscale resolution and portability provide significant advantages over the existing ORPAMs for biomedical and clinical research. Compared with the conventional scanning mechanisms, pORPAM offers a large FOV and removes the need for translation of samples/interfaces without sacrificing imaging quality and speed, yet with inhomogeneous sampling pattern over the entire FOV and sacrifice in axial resolution. We anticipate that improvement of axial resolution could be achieved by using a high-frequency cylindrically focused transducer and shifting the rotational centerline to the edge of the transducer. The portable and versatile configuration with minimal trade-offs regarding the convenience eliminates the motion artifacts introduced by hand compared to fully portable ORPAMs [21, 22]. More advanced implementations of pORPAM could

include utilization of lasers with a higher repetition rate to increase the imaging speed, use of compact brushless direct current (DC) rotary motors instead of the step motor to reduce the size of the imaging interface, and employing multiwavelength strategy to derive vascular functions [29, 30]. In terms of the imaging speed, it is primarily limited by the laser repetition rate. Commercially available lasers could feasibly emit over 1 500 000 pulses/s, which could significantly reduce the time cost to 0.5 second for 1 volume.

pORPAM makes it appropriate for broad applications, many of which are inaccessible to the conventional ORPAMs. We demonstrate classical and original applications of pORPAM in small-sized and multisized rodents as well as in human.

Mouse is an important animal model for studying a wide range of human diseases. Mouse ear has the features of thin, transparent and extremely complicated vasculatures, making it appropriate for many vascular studies [31, 32, 34–36]. Mouse brain has been extensively investigated to explore various brain diseases, disorders and functions [12, 35–40]. *in vivo* imaging of mouse ear and brain demonstrate that pORPAM has the comparable system performance to the conventional ORPAMs in classical applications.

The conventional ORPAMs suffer from major challenges in imaging medium- and large-sized rodents subjecting to translation and restriction of the animals as well as the limited FOV. pORPAM is able to be oriented in any direction for applications in many complicated sittings of the animals. As illustrated in Figure 4A, there is no need to translate or restrict rabbits, avoiding artifacts caused by animal struggling and mechanical vibration. pORPAM provides a large cylindrical FOV of 7×1.5 mm in 35 s with a moderate tradeoff in spatial resolution, which is still sufficient for vascular studies in medium- and large-sized rodents.

ORPAM has not found an appropriate clinical application so far. Oral diseases including ulcer, oral cancer and mucosal infections are relevant to superficial mucosal vasculatures that are readily accessible to ORPAM. However, it is challenging for the existing ORPAMs to inspect oral cavities limited by the size and compatibility of the imaging

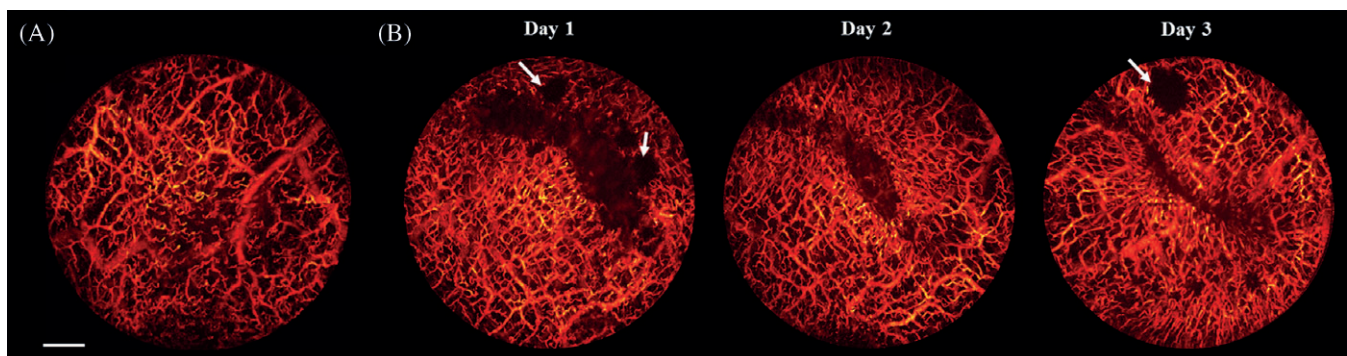


FIGURE 5 *In vivo* pORPAM imaging of oral vasculature in volunteers. (A) An MAP image of the vascular networks in a healthy human lip. (B) The recovery progress of an oral ulcer in the lip of a volunteer. The dark areas indicated by the white arrows were unexpected air bubbles between the human lip and imaging interface. Scale bars: 1 mm

interface. pORPAM equipped with a specially designed interface successfully captures the volumetric vascular networks in human lip. As illustrated in Figure 5, there are a tremendous amount of capillary loops on the top surface of the lip which might change during the early stage of cancerization. Thus, pORPAM has the potential to become a clinical tool for early stage diagnosis of oral cancer.

5 | CONCLUSION

In summary, we present a portable ORPAM system, and fully assess its capabilities by imaging a series of targets including phantom, mouse ears, mouse brains, rabbit ears, rabbit eyes and human lips. All these results show that our low-cost pORPAM prototype is compact, easy-to-use and widely applicable to multiscale organisms. We have demonstrated both classical and original applications in mice, rabbits and humans. We can envisage many other applications, ranging from lower organisms such as zebrafish and *Drosophila* to advanced rodents such as canines and primates.

ACKNOWLEDGMENTS

This work was funded by the National Natural Science Foundation of China 81571722 (Xi), 61775028 (Xi) and 61528401 (Xie and Xi), State International Collaboration Program from Sichuan 2016HH0019 (Xi), the start-up grant A03012023601011 (Xi) from University of Electronic Science and Technology of China. The authors thank the volunteers for participating in the human experiments.

AUTHOR BIOGRAPHIES

Please see Supporting Information online.

ORCID

Lei Xi  <http://orcid.org/0000-0002-2598-6801>

REFERENCES

- [1] V. Ntziachristos, *Nat. Methods* **2010**, *7*, 603.
- [2] V. Ntziachristos, J. Ripoll, L. V. Wang, R. Weissleder, *Nat. Biotechnol.* **2005**, *23*, 313.
- [3] A. Oraevsky, A. Karabutov, in *Biomedical Photonics Handbook* (T. Vo-Dinh, USA, 2003), p. 3401–3434.
- [4] A. Taruttis, V. Ntziachristos, *Nat. Photonics* **2015**, *9*, 219.
- [5] P. Beard, *Interface Focus* **2011**, *1*, 602.
- [6] L. V. Wang, *Nat. Photonics* **2009**, *3*, 503.
- [7] R. Kruger, R. Lam, D. Reinecke, S. Del Rio, R. Doyle, *Med. Phys.* **2010**, *37*, 6096.
- [8] R. Ma, S. Söntges, S. Shoham, V. Ntziachristos, D. Razansky, *Biomed. Opt. Exp.* **2012**, *3*, 1724.
- [9] H. Estrada, J. Turner, M. Kneipp, D. Razansky, *Laser Phys. Lett.* **2014**, *11*, 045601.
- [10] A. Taruttis, G. Dam, V. Ntziachristos, *Cancer Res.* **2015**, *75*, 1548.
- [11] A. P. Jathoul, A. P. Jathoul, J. Laufer, O. Ogunlade, B. Treeby, B. Cox, E. Zhang, P. Johnson, A. R. Pizzey, B. Philip, T. Marafioti, M. F. Lythgoe, R. B. Pedley, M. A. Pule, P. Beard, *Nat. Photonics* **2015**, *9*, 239.
- [12] M. Kircher, A. Zerda, J. V. Jokerst, C. L. Zavaleta, P. J. Kempen, E. Mitra, K. Pitter, R. Huang, C. Campos, F. Habte, R. Sinclair, C. W. Brennan, I. K. Mellinghoff, E. C. Holland, S. S. Gambhir, *Nat. Med.* **2012**, *18*, 829.
- [13] S. Manohar, S. E. Vaartjes, J. C. G. van Hesperen, J. M. Klaase, F. M. van den Engh, W. Steenbergen, T. G. van Leeuwen, *Opt. Express* **2007**, *15*, 12277.
- [14] X. Deánben, G. Sela, A. Lauri, M. Kneipp, V. Ntziachristos, G. Westmeyer, S. Shoham, D. Razansky, *Light Sci. Appl.* **2016**, *5*.
- [15] S. Ermilov, T. Khamapirad, A. Conjusteau, M. H. Leonard, R. Laceywell, K. Mehta, T. Miller, A. A. Oraevsky, *J. Biomed. Opt.* **2009**, *14*, 024007.
- [16] H. Zhang, K. Maslov, G. Stoica, L. V. Wang, *Nat. Biotechnol.* **2006**, *24*, 848.
- [17] S. Hu, K. Maslov, L. V. Wang, *Opt. Lett.* **2011**, *36*, 1134.
- [18] H. Wang, X. Yang, Y. Liu, B. Jiang, Q. Luo, *Opt. Express* **2013**, *21*, 24210.
- [19] W. Song, W. Zheng, R. Liu, R. Lin, H. Huang, X. Gong, S. Yang, R. Zhang, L. Song, *Biomed. Opt. Express* **2014**, *12*, 4235.
- [20] L. Lin, P. Zhang, S. Xu, J. Shi, L. Li, J. Yao, L. Wang, J. Zou, L. V. Wang, *J. Biomed. Opt.* **2017**, *22*, 41002.
- [21] J. Kim, C. Lee, K. Park, G. Lim, C. Kim, *Sci. Rep.* **2015**, *5*, 7932.
- [22] P. Hajireza, W. Shi, A. Forbrich, P. Shao, R. Zemp, *Proc. SPIE* **2012**, *8223*, 82230I-1.
- [23] Y. Yuan, S. Yang, D. Xing, *Appl. Phys. Lett.* **2012**, *100*, 023702.
- [24] H. Kang, S. Lee, E. Lee, S. Kim, T. Lee, *Biomed. Opt. Express* **2015**, *6*, 4650.
- [25] L. Li, C. Yeh, S. Hu, L. Wang, B. T. Soetikno, R. Chen, Q. Zhou, K. K. Shung, K. I. Maslov, L. V. Wang, *Opt. Lett.* **2014**, *39*, 2117.
- [26] B. Rao, L. Li, K. Maslov, L. Wang, *Opt. Lett.* **2010**, *35*, 1521.
- [27] W. Qi, T. Jin, J. Rong, H. Jiang, L. Xi, *J. Biophotonics* **2017**, *10*, 950.
- [28] J. Takano, T. Yakushiji, I. Kamiyama, T. Nomura, A. Katakura, N. Takano, T. Shibahara, *Int. J. Oral Maxillofac. Surg.* **2010**, *39*, 208.
- [29] P. Hajireza, A. Forbrich, R. Zemp, *Biomed. Opt. Express* **2014**, *5*, 539.
- [30] S. Hu, K. Maslov, V. Tsytarev, L. V. Wang, *J. Biomed. Opt.* **2009**, *14*, 040503.
- [31] L. Wang, K. Maslov, L. V. Wang, *Proc. Natl. Acad. Sci. U.S.A.* **2013**, *110*, 5759.
- [32] Z. Luo, P. Wang, A. Zhang, G. Zuo, Y. Zheng, Y. Huang, *PLoS One* **2015**, *10*, e0116076.
- [33] H. Inoue, M. Kaga, H. Ikeda, C. Sato, H. Sato, H. Minami, E. G. Santi, B. Hayee, N. Eleftheriadis, *Ann. Gastroenterol.* **2015**, *28*, 41.
- [34] S. Oladipipo, S. Hu, A. Santeford, J. Yao, J. Kovalski, R. Shohet, K. Maslov, L. V. Wang, *J. Arbeit, Blood* **2011**, *117*, 4142.
- [35] P. Hai, Y. Zhou, R. Zhang, J. Ma, Y. Li, J. Shao, L. V. Wang, *J. Biomed. Opt.* **2017**, *22*, 41004.
- [36] R. Cao, J. Li, B. Ning, N. Sun, T. Wang, Z. Zuo, S. Hu, *NeuroImage* **2017**, *150*, 77.
- [37] W. Lu, Q. Huang, G. Ku, X. Wen, M. Zhou, D. Guzatov, P. Brecht, R. Su, A. Oraevsky, L. V. Wang, C. Li, *Biomaterials* **2010**, *31*, 2617.
- [38] L. Xiang, L. Ji, T. Zhang, B. Wang, J. Yang, Q. Zhang, M. S. Jiang, J. Zhou, P. R. Carney, H. Jiang, *Neuroimage* **2013**, *66*, 240.
- [39] A. Zerda, C. Zavaleta, S. Keren, S. Vaithilingam, S. Bodapati, Z. Liu, J. Levi, B. R. Smith, T. Ma, O. Oralkan, Z. Cheng, X. Chen, H. Dai, B. T. Khuri-Yakub, S. S. Gambhir, *Nat. Nanotechnol.* **2008**, *3*, 557.
- [40] R. Lin, J. Chen, H. Wang, M. Yan, W. Zheng, L. Song, *Quant. Imaging Med. Surg.* **2015**, *5*, 23.

SUPPORTING INFORMATION

Additional Supporting Information may be found online in the supporting information tab for this article.

Figure S1. The layout of the CUPAM configuration. CFT, cylindrically focused transducer; DAQ, data acquisition card; GVS, galvanometer scanner; OL, objective; PC, Personal computer; PH, pinhole; R, rotator; SL, scan lens; SMF, single-mode fiber

Figure S2. The photographs of the mouse in the experiments of (A) brain and (B) ear imaging

Movie S1. Scanning mechanism of pORPAM.

Movie S2. The volume rendering of a mouse brain imaged by the low-resolution mode in different views and cross-sectional slices at different depths.

Movie S3. The volume rendering of a mouse brain imaged by the high-resolution mode in different views and cross-sectional slices at different depths.

Movie S4. Volumetric rendering and slices of the vascular network at different depths in a human lip.

How to cite this article: Jin T, Guo H, Yao L, Xie H, Jiang H, Xi L. Portable optical-resolution photoacoustic microscopy for volumetric imaging of multiscale organisms. *J. Biophotonics*. 2017; e201700250. <https://doi.org/10.1002/jbio.201700250>